第36卷第3期 2017年6月
红外与毫米波学报 J. Infrared Millim. Waves
Vol. 36, No. 3 June, 2017

文章编号: 1001-9014(2017)03-0261-06 DOI: 10.11972/j.issn.1001-9014.2017.03.002

Tunable metamaterial Terahertz band-stop filter based on InSb

BAI Yu-Kun[1,2*], WEI Ren-Xiao[1], MA Xiu-Rong[1], MA Ying[1]

(1. School of Electrial and Electronic Engineering, Tianjin University of Technology, Tianjin 300384, China;
2. Institute of Laser and Optoelectronics, Tianjin University, Tianjin 300072, China)

Abstract: A metamaterial band-stop filter in the Terahertz (THz) spectrum regime based on the semiconductor InSb is presented in this paper. The resonant frequency of the filter is thermally tunable due to the dielectric constant properties of InSb. Meanwhile, the effects of geometrical parameters on the performance of the filter were analyzed by the finite-integral method and equivalent LMC circuit method, respectively. The results of the two methods show good agreement with each other. The resonant frequency can be dynamically tuned across a wide band of frequencies from 0.91 to 1.28 THz in the temperature range from 220 K to 350 K, and the transmission coefficient at the resonant frequency in the stopband can be effectively suppressed. Good incidence-angle stability of the transmission characteristics up to an oblique incidence angle of 30° is demonstrated. The tunable metamaterial band-stop filter has the potential to be applied in the Terahertz wireless communication and sensing systems.

Key words: band-stop filter, metamaterial, InSb, Terahertz
PACS: 41.20.Jb, 78.20.Ci, 42.25.Bs

基于锑化铟的可调超材料太赫兹带阻滤波器

白育堃[1,2*], 魏仁霄[1], 马秀荣[1], 马 颖[1]
(1. 天津理工大学 电气电子工程学院,天津 300384;
2. 天津大学 激光与光电子研究所,天津 300072)

摘要:提出了一种工作在太赫兹频段,基于半导体材料锑化铟的超材料带阻滤波器.由于锑化铟材料介电常数的特性,该滤波器的谐振频率能够进行温度调节.同时,通过有限积分法和等效LMC电路模型分析了滤波器的几何参数对其谐振频率的影响,这两种方法得到的结果具有良好的一致性.在温度的取值范围是220~350 K时,滤波器的谐振频率能够从0.91 THz动态调节到1.28 THz,并且其阻带谐振频率的透射系数能够有限地被抑制.该滤波器的传输特性在30°入射角范围内具有良好的稳定性.设计的可调超材料带阻滤波器将在太赫兹无线通信、传感等方面有潜在的应用前景.

关 键 词:带阻滤波器;超材料;锑化铟;太赫兹

中图分类号:TN713.5 **文献标识码**:A

Introduction

Terahertz technology has emerged to be one of the most rapidly developing research area in recent years[1-2]. Because natural materials of strong electromagnetic responses in the Terahertz frequency regime are scarce, metamaterial based Terahertz devices have come into existence. Metamaterial is composed of subwavelength microstructures which can be designed to implement functions inaccessible to natural materials in devices such as filter[3], modulator[4], sensor[5], isolator[6], and negative-refraction-index enabled devices[7-9], and so on.

Quan Li *et al.*[10] designed a band-stop filter based on the rectangular split ring resonator (SRR) with adjustable resonant frequencies by changing the relative distance between two SRRs. An effective equivalent circuit model was proposed to reveal its physical explanation. Kadir *et al.*[11] presented a new metamaterial

Received date: 2016-07-11, **revised date**: 2016-12-07 **收稿日期**:2016-07-11, **修回日期**:2016-12-07
Foundation items: The National Natural Science Foundation of China (.11004152), The National 973 Plan of China (2010CB327801)
Biography: BAI Yu-Kun (1970-), male, Shanxi, associate professor, Ph. D. Research fields mainly focus on optical communication and terahertz technology.
* **Corresponding author**: E-mail: tjutbai_1@163.com

broadband absorber in X-band, which had two minimums at the frequencies of 9.10 GHz and 10.53 GHz due to two different SRRs. It was observed that increasing the number of unit cells makes absorption level smoother. Wang *et al.* [12] investigated a photo-excited THz switch based on a new rectangular SRR structure and photosensitive silicon. With a light excitation, the band-stop filtering effect was demonstrated as a result of the increase of carrier concentration. SRRs play a vital role in the metamaterial structures to construct filters.

A metamaterial based on the two-dimensional-array of rectangular SRRs loaded with thermally-sensitive semiconductor InSb was introduced to construct the dynamically tunable THz band-stop filter in this paper. Compared with the previous researches[13-14], improvements in terms of the equivalent circuit analysis and the incidence-angle stability of the filter were achieved. Finite-integral method based commercial simulation software CST was used for investigating the filter's performances including the incidence-angle stability. Comparison was made with the equivalent LMC circuit method, which shows the physical insight of its operation principle.

1 Structure of the THz metamaterial band-stop filter

The top view of the two-dimensionally periodic array structure of the filter is shown in Fig. 1(a). It consists of the dielectric substrate, i.e. Rogers RT6002 (tm) with dielectric constant 2.94, loss tangent 0.0012 and thickness $h = 200$ μm; gold rectangular SRRs and separation lines with thickness $t = 0.5$ μm and electrical conductivity 4.09×10^7 s/m on top surface of the substrate. InSb is loaded inside the rectangular SRRs with thickness t = 0.5 μm.

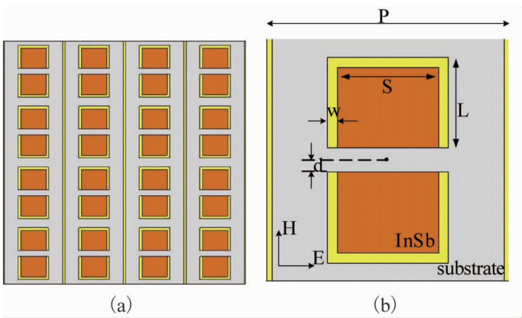

Fig. 1 Top view of the THz filter structure, (a) 2-D periodic array, (b) unit cell
图1 太赫兹滤波器的俯视图 (a)二维阵列 (b)单元结构

The square unit cell of the periodic structure is shown in Fig. 1(b). Geometrical parameters of the figure are as follows: side length of the square substrate P = 120 μm, horizontal inner length of the rectangular SRR S = 40 μm, half length of the split vertical side of the rectangular SRR L = 45 μm, metal line width w = 5 μm, and half width of the gap between the upper and lower parts of the SRR d = 2 μm. The thermally-sensitive InSb is between the upper and lower parts of the rectangular SRR.

2 Equivalent LMC circuit Model

The unit cell can be analyzed by the equivalent LMC circuit model, as shown in Fig. 2. The resonant circuit consists of self-inductances L_1 and L_2, capacitance C_1 and mutual inductances M_1, M_2 and M_3, with M_3 being the mutual inductance between two adjacent unit cells.

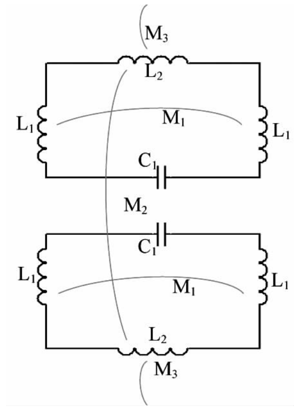

Fig. 2 Equivalent circuit model of the unit structure
图2 单元结构的等效电路模型

The parameters of the lumped equivalent circuit components in the model can be analytically calculated. According to the Bueno principle[15], the self-induction of a metal bar is determined through the ratio of its length L_0 to width w as:

$$\Lambda(L_0) = \frac{\mu_0 L_0}{4\pi}\{2\sinh^{-1}(\frac{L_0}{w}) + 2(\frac{L_0}{w})\sinh^{-1}(\frac{w}{L_0}) + \frac{2}{3}[(\frac{L_0}{w})^2 + \frac{w}{L_0} - \frac{(w^2+L_0^2)^{2/3}}{L_0 w^2}]\} \quad ,(1)$$

where $\mu_0 = 4\pi\times10^{-7}$ H/m is the permeability of free space. Here, the self-inductances L_1 and L_2 can be calculated as $L_1 = \Lambda(L-w)$ and $L_2 = \Lambda S$.

Generic formula of mutual inductance between two parallel identical metal bars with length L_0, separation h_0 between them, and current densities in the same direction can be written as[15]:

$$\Xi(L_0,h_0) = \frac{\mu_0}{4\pi}\{2L_0\sinh^{-1}(\frac{L_0}{h_0}) + 2[h_0 - (L_0^2+h_0^2)^{1/2}]\} \quad ,(2)$$

$M_1 = -\Xi(L-w, S-w)$, $M_2 = \Xi(S, 2L+2d-w)$ and $M_3 = \Xi(S, P-2L-2d+w)$, where the negative sign in M_1 is an indication of opposite surface current direction.

Based on the line capacitance theory[16], the value of capacitor C_1 can be formulated as:

$$C_1 = \alpha\varepsilon_0\varepsilon_{\text{eff}}(L-w)\frac{K(k'_0)}{K(k_0)} \quad ,(3)$$

where ε_0 is the permittivity of free space, $\varepsilon_{\text{eff}} = \beta\varepsilon_{\text{sub}} + (1-\beta)\varepsilon_{\text{InSb}}$ is the effective complex dielectric constant of the composite of InSb and substrate, and K the complete elliptic integral of the first kind with $k_0 = S/(S+2w)$ and $k'_0 = \sqrt{1-k_0^2}$. Here α and β are two unknown constants.

The mutual inductance between a metal separation line and adjacent SRRs is very small, leading to negligible effects on the filtering performance except for a little lowering of the transmission in the stop-band. Taking into account of the significant contributions and ignoring all the losses, the impedance of the equivalent circuit Z_m can be written as:

$$z_m = j\omega(M_2 + M_3) + \left[\frac{1}{j\omega C_1} + j\omega(2L_1 + L_2 + 2M_1)\right] \quad . \quad (4)$$

Imposing the resonance condition Im $(Z_m) = 0$, the resonant frequency of the bandstop filter can be derived as:

$$f_0 = \frac{1}{2\pi\sqrt{(2L_1 + L_2 + 2M_1 + M_2 + M_3)C}} \quad , \quad (5)$$

$$C = \frac{\mathrm{Re}^2(C_1) + \mathrm{Im}^2(C_1)}{\mathrm{Re}(C_1)} \quad . \quad (6)$$

Through Eqs. (3) and (5), it is easily found that tuning the dielectric constant of InSb can change the capacitor C_1, hence the resonant frequency f_0, realizing a dynamic tunable Terahertz bandstop filter. Dielectric constant of InSb can be calculated from Drude[17-19] model

$$\varepsilon_{\mathrm{InSb}}(\omega) = \varepsilon_\infty - \omega_p^2/(\omega^2 + i\gamma\omega) \quad , \quad (7)$$

where ε_∞ is the high frequency limit, γ the damping factor, and ω_p the plasma frequency. ω_p is calculated from

$$\omega_p = \sqrt{\frac{Ne^2}{\varepsilon_0 m^*}} \quad , \quad (8)$$

where the intrinsic carrier density N, the electron charge e, the effective mass $m*$ of free carriers and the free-space permittivity ε_0. The intrinsic carrier density N (m^{-3}) of InSb is

$$N = 5.76 \times 10^{20} T^{3/2} e^{-0.26/(2k_B T)} \quad , \quad (9)$$

where k_B is the Boltzmann constant, T the temperature in unit of kelvin. Calculated from Eqs. (8-9), the dielectric constant of InSb versus frequency at different temperatures is shown in Fig. 3 with $\varepsilon_\infty = 15.68$, $\gamma = 2\pi \times 0.05$ THz, $m^* = 0.015 m_e$ and $m_e = 9.1 \times 10^{-3}$ kg.

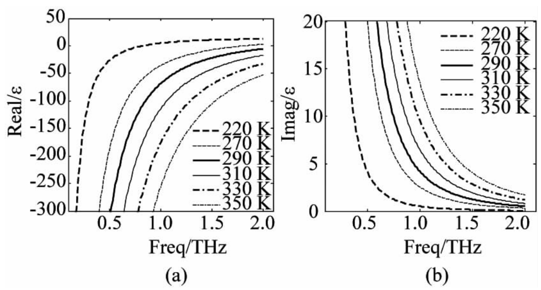

Fig. 3　Dielectric constant of InSb. (a) real part and (b) imaginary part, at different temperatures

图 3　不同温度下的 InSb 的介电常数 (a)实部(b)虚部

3　Simulation and equivalent circuit analysis results

To highlight the influence of temperature, the range of temperature under concern is 220 ~ 350 K. With a normal incident THz wave, the transmission spectra of the band-stop filter obtained by simulations are presented in Fig. 4. It is observed that the resonant frequency increases with temperature and can be dynamically tuned across a wide band of frequencies from 0.91 THz to 1.28 THz in the temperature range from 220 K to 350 K. As indicated by Eq. (5), the increase of temperature, which gives rise to the variation of effective capacitance, leads to the blue shift of the resonant frequency. Furthermore, the transmission coefficients at resonant frequencies are effectively suppressed.

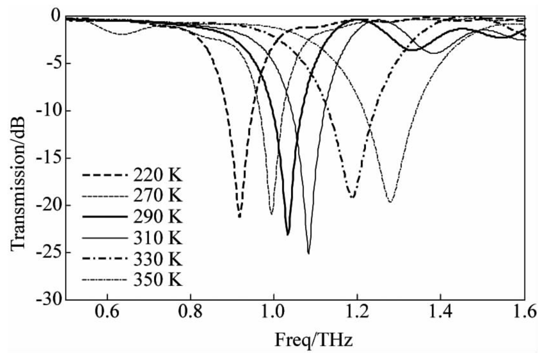

Fig. 4　Transmission spectra at different temperatures

图 4　不同温度的透射谱

The electric field distributions at resonant frequencies corresponding to the temperatures of 220 K, 310 K and 350 K on the unit cell are shown in Fig. 5. At lower temperature, the electric field distributes mainly in the split ring region of the SRR. When the temperature increases, the electric field in the split region of InSb increases. In other words, the temperature increase leads to the InSb carrier concentration increase, hence the dominance of its metal characteristics.

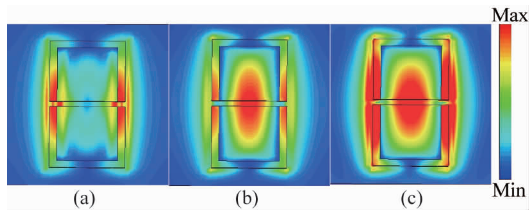

Fig. 5　The distributions of electric field at the resonant frequencies corresponding to various temperatures (a) 220 K, 0.918 THz, (b) 310 K, 1.083 THz, (c) 350 K, 1.279 THz

图 5　不同温度下谐振频率对应的电场分布图 (a) 220 K, 0.918 THz, (b) 310 K, 1.083 THz, (c) 350 K, 1.279 THz

While the resonant frequency can be dynamically tuned with temperature due to the load of InSb, it can also be adjusted by the geometrical parameters of the rectangular SRR structure. Geometrical parameters that have a significant impact on the filtering characteristics, including the gap width d, horizontal bar length S, and vertical bar length L, were investigated at $T = 220$ K.

Firstly, the gap width d of the structure was varied among 2, 4, 6 and 8 μm. The corresponding transmission spectra calculated by simulations are shown in Fig. 6 (a). As shown in the figure, the resonant frequency changes from 0.95 to 0.85 THz as d is varied from 2 to 8 μm. The resonant frequency decreases with the increase of d.

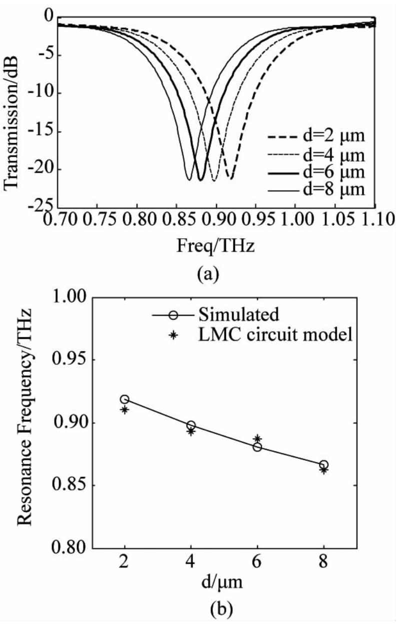

Fig. 6 (a) Transmission spectra and (b) resonant frequencies calculated by simulations and equivalent circuit model for different values of d

图6 不同 d 对应的透射谱以及谐振频率(a)透射谱,(b)通过仿真和等效电路得到的谐振频率

Using the equivalent LMC circuit model, the two unknown constants α and β can be derived as $\alpha = 0.112$ and $\beta = 0.98$ by fitting the analytical resonance wavelengths calculated from Eq. (5) to the simulation results shown in Fig. 4. Various circuit parameters for different values of d were calculated in Table 1. It is evident that self-inductances L_1 and L_2, mutual inductance M_1 and capacitance C_1 remain invariable, whereas mutual inductances M_1 and M_2 change as d is varied. Resonant frequencies calculated by Eq. (5) were compared with the simulation results in Fig. 6(b), in which the solid line with open circles was obtained by simulations and asterisks were calculated by the equivalent circuit model.

Secondly, the horizontal bar length S of the structure was varied among 40, 50, 60 and 70 μm. The corresponding transmission spectra calculated by simulations are shown in Fig. 7(a). As shown in the figure, the filter resonant frequency decreases with the increase of S.

Using the equivalent LMC circuit model, various circuit parameters for different values of S were calculated in Table 2. It was found that only self-inductance L_1 remains constant as S varies. Resonant frequencies calculated by Eq. (5) were compared with the simulation results in Fig. 7(b).

Table 1 Obtained Circuit Parameters in the LMC Model for Various Values of d

表1 利用 LMC 模型得到不同 d 值对应的电路参数

d /μm	2	4	6	8
L_1/pH	26.509	26.509	26.509	26.509
L_2/pH	26.509	26.509	26.509	26.509
M_1/pH	-4.200 8	-4.200 8	-4.200 8	-4.200 8
M_2/pH	1.769 2	1.695 3	1.627 2	1.564 4
M_3/pH	4.659 0	5.223 6	5.935 7	6.861 3
Re(C_1) /fF	0.407 1	0.407 1	0.407 1	0.407 1
Im(C_1) /fF	0.003 2	0.003 2	0.003 2	0.003 2

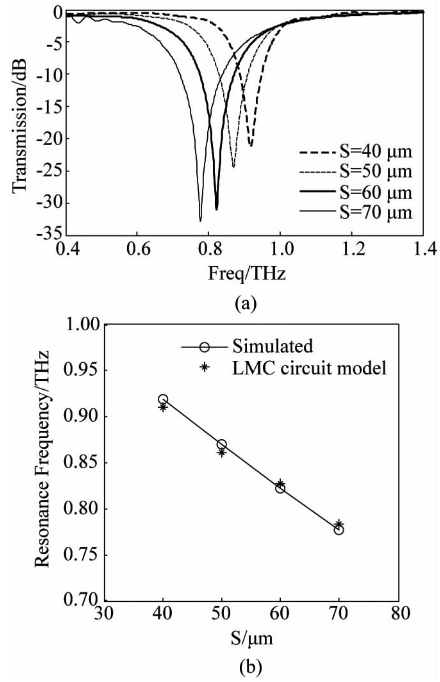

Fig. 7 (a) Transmission spectra and (b) resonant frequencies calculated by simulations and equivalent circuit model for different values of S 图7 不同 S 对应的透射谱以及谐振频率(a)透射谱,(b)通过仿真和等效电路得到的谐振频率

Table 2 Obtained Circuit Parameters in the LMC Model for Various Values of S

表2 利用 LMC 模型得到不同 S 值对应的电路参数

S/μm	40	50	60	70
L_1/pH	26.509	26.509	26.509	26.509
L_2/pH	26.509	35.286	44.466	53.981
M_1/pH	-4.200 8	-3.363 1	-2.797 5	-2.391 4
M_2/pH	1.769 2	2.741 3	3.909 2	5.263 5
M_3/pH	4.659 0	6.992 0	9.665 8	12.636 6
Re(C_1) /fF	0.407 1	0.374 0	0.350 6	0.343 2
Im(C_1) /fF	0.003 2	0.002 9	0.002 8	0.002 7

Thirdly, the vertical bar length L of the structure was varied among 31, 38, 45 and 52 μm, The corresponding transmission spectra calculated by simulations are shown in Fig. 8(a). As shown in the figure, the filter resonant frequency decreases with the increase of L. The resonant frequency is more sensitive to the vertical bar length L than to the horizontal bar length S.

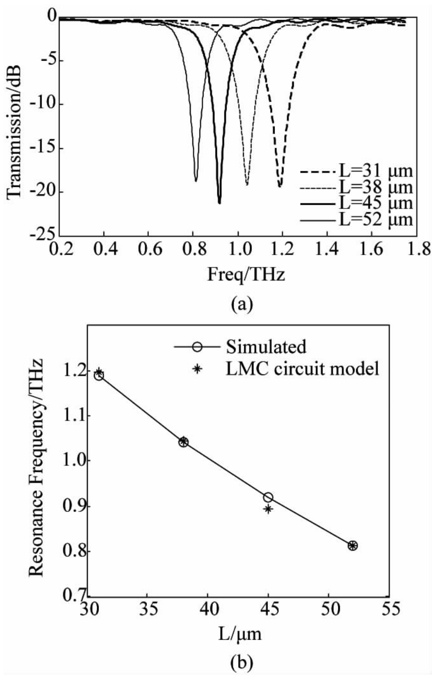

Fig. 8 (a) Transmission spectra and (b) resonant frequencies calculated by simulations and equivalent circuit model for different values of L

图 8　不同 L 对应的透射谱以及谐振频率 (a)透射谱, (b)通过仿真和等效电路得到的谐振频率

Using the equivalent LMC circuit model, various circuit parameters for different values of L were calculated in Table 3. It was found that only self-inductance L_2 remains constant as L varies. Resonant frequencies calculated by Eq. (5) were compared with the simulation results in Fig. 8(b).

Table 3　Obtained Circuit Parameters in the LMC Model for Various Values of L

表 3　利用 LMC 模型得到不同 L 值对应的电路参数

L /μm	31	38	45	52
L_1/pH	15.103	20.656	26.509	32.607
L_2/pH	26.509	26.509	26.509	26.509
M_1/pH	−1.854 5	−2.925 7	−4.200 8	−5.660 5
M_2/pH	2.539 2	2.086 6	1.769 2	1.534 7
M_3/pH	2.620 0	3.363 1	4.659 0	7.761 6
Re(C_1) /fF	0.304 3	0.344 2	0.407 1	0.427 9
Im(C_1) /fF	0.002 4	0.002 7	0.003 2	0.003 6

The incidence-angle stability of the filter was investigated for oblique incidence of THz waves. In the case of horizontal polarizations, the transmission spectra for the incidence angles from 10° to 60° are shown in Fig. 9 with reference to that of normal incidence. As shown in the figure, the resonant frequencies for all the oblique incidence angles are practically identical, i. e. 0. 918 THz. The bandwidth change is insignificant up to the incidence angle 30°. Afterwards, the bandwidth increases dramatically with the increase of incidence angle. Therefore, the filter has very good resonant frequency stability up to the incidence angle of 60° and the overall filtering characteristics are fairly stable up to the incidence angle of 30°.

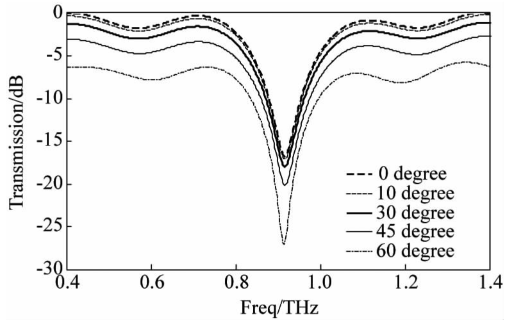

Fig. 9　Transmission spectra at different incidence angles

图 9　入射角不同时对应的透射谱

4　Conclusions

A dynamically tunable band-stop filter in the THz spectrum regime is presented in this paper. The temperature-dependent dielectric constant of InSb loaded into the rectangular SRR enables the wideband tunability of the filter. Geometrical parameters of the unit cell are also effective in tuning the resonant frequency to various extents, which can be determined in accordance with the operating frequency band. Simulation results show fairly good agreement with that of the equivalent LMC circuit model. The filtering characteristics are reasonably good for a narrowband band-stop filter with stable performance for oblique incidence angles less than 30°. The dynamically tunable band-stop filter constructed with a simple structure can find applications in the Terahertz communication and sensing systems.

References

[1] Claus R. Electrons catch a terahertz wave [J]. *Science*, 2016, **352**(6284): 410−411.

[2] Masanori H. Development and future prospects of terahertz technology [J]. *Japanese Journal of Applied Physics*, 2015, **54**(12): 1−16.

[3] Zhong M, Han G M. Tunable broad stop-band filter based on multilayer metamaterials in the THz regime [J]. *J. Infrared Millim. Waves*, 2016, **35**(1): 11−15.

[4] Mao Q, Wen Q Y, Tian W, *et al.* High-speed and broadband terahertz wave modulators based on large-area grapheme field-effect transistors [J]. *Optics Letters*, 2014, **39**(19): 5649−5652.

[5] Liu Y, Zhang Y Q, Jin X R, *et al.* Dual-band infrared perfect absorber for plasmonic sensor based on the electromagnetically induced reflection-like effect [J]. *Optics Communications*, 2016, **371**: 173−177.

[6] Chen S, Fan F, Wang X H, *et al.* Terahertz isolator based on nonreciprocal magneto metasurface [J]. *Optics Express*, 2015, **23**(2): 1015−1024.

(下转第 275 页)

both the electron-electron scattering and the electron-phonon scattering play important roles in the Te-doped sample.

References

[1] Hasan M Z, Kane C L. Colloquium: topological insulators [J]. *Reviews of Modern Physics*, 2010, **82**: 3045 – 3067.
[2] Qi X L, Zhang S C. Topological insulators and superconductors [J]. Reviews of Modern Physics, 2011, **83**: 1057 – 1110.
[3] Hsieh D, Xia Y, Qian D, *et al.* A tunable topological insulator in the spin helical Dirac transport regime [J]. *Nature*, 2009, **460**: 1101 – 1105.
[4] Analytis J G, McDonald R D, Riggs S C, *et al.* Two-dimensional surface state in the quantum limit of a topological insulator [J]. *Nature Physics*, 2010, **6**: 960 – 964.
[5] Ren Z, Taskin A A, Sasaki S, *et al.* Large bulk resistivity and surface quantum oscillations in the topological insulator Bi_2Te_2Se [J]. *Physical Review B*, 2010, **82**: 241306.
[6] Xiong J, Petersen A C, Qu D X, *et al.* Quantum oscillations in a topological insulator Bi_2Te_2Se with large bulk resistivity (6 Ω · cm) [J]. *Physica E*, 2012, **44**: 917 – 920.
[7] Xiong J, Luo Y K, Khoo Y H, *et al.* High-field Shubnikov – de Haas oscillations in the topological insulator Bi_2Te_2Se [J]. *Physical Review B*, 2012, **86**: 045314.
[8] Peng H L, Lai K J, Kong D S, *et al.* Aharonov – Bohm interference in topological insulator nanoribbons [J]. *Nature Materials*, 2010, **9**: 225 – 229.
[9] Kong D S, Rande J C, Peng H L, *et al.* Topological insulator nanowires and nanoribbons [J]. Nano Letters, 2010, **10**: 329 – 333.
[10] Kong D S, Dang W H, Cha J J, *et al.* Few-layer nanoplates of Bi_2Se_3 and Bi_2Te_3 with highly tunable chemical potential [J]. *Nano Letters*, 2010, **10**: 2245 – 2250.
[11] Hong S S, Cha J J, Kong D S, *et al.* Ultra-low carrier concentration and surface dominant transport in antimony-doped Bi_2Se_3 topological insulator nanoribbons [J]. *Nature Communications*, 2012, **3**: 757.
[12] Cha J J, Kong D S, Hong S S, *et al.* Weak antilocalization in $Bi_2(Se_xTe_{1-x})_3$ nanoribbons and nanoplates [J]. *Nano Letters*, 2012, **12**: 1107 – 1111.
[13] Tang H, Liang D, Qiu Richard L J, *et al.* Two-dimensional transport induced linear magneto-resistance in topological insulator Bi_2Se_3 nanoribbons [J]. *ACS Nano*, 2011, **5**: 7510 – 7516.
[14] Gehring P, Gao B, Burghard M, *et al.* Two-dimensional magneto-transport in Bi_2Te_2Se nanoplatelets [J]. *Applied Physics Letters*, 2012, **101**: 023116.
[15] Liu M H, Chang C Z, Zhang Z C, *et al.* Electron interaction-driven insulating ground state in Bi_2Se_3 topological insulators in the two-dimensional limit [J]. *Physical Review B*, 2011, **83**: 165440.
[16] Kim Y S, Brahlek M, Bansa N, *et al.* Thickness-dependent bulk properties and weak antilocalization effect in topological insulator Bi_2Se_3[J]. *Physical Review B*, 2011, **84**: 073109.
[17] Chen J, He X Y, Wu K H, *et al.* Tunable surface conductivity in Bi_2Se_3 revealed in diffusive electron transport [J]. *Physical Review B*, 2011, **83**: 241304.
[18] Zhang G, Qin H, Chen J, *et al.* Growth of Topological Insulator Bi_2Se_3 Thin Films on $SrTiO_3$ with Large Tunability in Chemical Potential [J]. *Advanced Functional Materials*, 2011, **21**: 2351 – 2355.
[19] Hamdou B, Gooth J, Dorn A, *et al.* Surface state dominated transport in topological insulator Bi_2Te_3 nanowires [J]. *Applied Physics Letters*, 2013, **103**: 193107.
[20] Hikami S, Larkin A I, Nagaoka Y. Spin-orbit interaction and magnetoresistance in the two dimensional random system [J]. *Progress of Theoretical Physics*, 1980, **63**: 707.
[21] Bayot V, Piraux L, Michenaud J P, *et al.* Two-dimensional weak localization in partially graphitic carbons [J]. *Physical Review B*, 1990, **41**: 11770.
[22] Wei L M, Liu X Z, Yu G L, *et al.* Antilocalization effect in HgCdTe film [J]. *J. Infrared Millim. Waves*, (魏来明, 刘新智, 俞国林, 等. HgCdTe 薄膜的反局域效应. **红外与毫米波学报**) 2013, **32**: 141 – 144.
[23] Altshuler B L, Aronov A G. Electron-electron interaction in disordered systems [M]. New York: Elsevier Science Publishing Company, 1985.
[24] Kallaher R L, Heremans J J. Spin and phase coherence measured by antilocalization in n-InSb thin films [J]. *Physical Review B*, 2009, **79**: 075322.
[25] Rammer J, Schmid A. Destruction of phase coherence by electron-phonon interactions in disordered conductors [J]. *Physical Review B*, 1986, **34**: 1352.
[26] Reizer M Yu, Electron-phonon relaxation in pure metals and superconductors at very low temperatures [J]. *Physical Review B*, 1989, **40**: 5411.

(上接第 265 页)
[7] Jia X L, Meng Q X, Yuan C X, *et al.* A novel chiral nano structure for optical activities and negative refractive index [J]. *Optik*, 2016, **127**(14): 5738 – 5742.
[8] Schurig D, Mock J J, Justice B J, *et al.* Metamaterial electromagnetic cloak at microwave frequencies [J]. *Science*, 2006, **314**(5801): 977 – 980.
[9] Patrick R, Cumali S. Wide-band polarization independent perfect metamaterrial absorber based on concentric ring topology for solar cells application [J]. *Journal of Alloys and Compounds*, 2016, **680**: 473 – 479.
[10] Li Q, Zhang X Q, Cao W, *et al.* An approach for mechanically tunable, dynamic terahertz bandstop filters[J]. *Applied Physics A*, 2012, **107**(2): 285 – 291.
[11] Kadir O, Okan M Y, Hasan K. Metamaterial based broadband RF absorber at X-band [J]. *Int. J. Electron. Commun.* (*AEU*), 2016, **70**(8): 1062 – 1070.
[12] Wang G C, Zhang J N, Zhang B, *et al.* Photo-excited terahertz switch based on composite metamaterial structure [J]. *Optics Communications*, 2016, **374**: 64 – 68.
[13] Hu J R, Li J S, Cheng W. Research on a thermally tunable terahertz wave band-stop filter based on thermo-sensitive media[J]. *Electronic components and materials*(胡建荣,李九生,程伟. 基于温敏介质的温控太赫兹波带阻滤波器研究. 电子元件与材料), 2014, **33**(5): 57 – 60.
[14] Cheng W. Research on tunable terahertz wave devices using metamaterials and photonic crystals[D]. Hang zhou: China Jiliang University (程伟. 基于电磁超材料和光子晶体的可调太赫兹波器件研究. 杭州:中国计量大学), 2014.
[15] Marcelo A B, Assis A K T. A new method for inductance calculations [J]. *J. Phys. D: Appl. Phys*, 1995, **28**(9): 1802 – 1806.
[16] Gevorgian S, Berg H. Line capacitance and impedance of coplanar-strip waveguides on substrates with multiple dielectric layers [J]. *In 31st European Microwave Conference*, 2001.
[17] Passmore B S, Allen D G, Vangala S R, *et al.* Mid-infrared doping tunable transmission through subwavelength metal hole arrays on InSb [J]. *Optics Express*, 2009, **17**(12): 10223 – 10230.
[18] Zhu J, Han J G, Tian Z, *et al.* Thermal broadband tunable Terahertz metamaterials [J]. *Optics Communications*, 2011, **284**: 3129 – 3133.
[19] Gu W H, Chang S J, Fan F, *et al.* InSb-based tunable terahertz directional beaming device [J]. *Optics Communications*, 2016, **377**: 110 – 114.